CO2 reduction on post-transition metals and their alloys: an industrial approach

Pavesi, D.

Appendix A

Supporting Information to Chapter 3: Cathodic disintegration as an easily scalable method for the production of Sn and Pb based catalysts for CO_2 reduction

A.1 Supplementary Figures and Tables

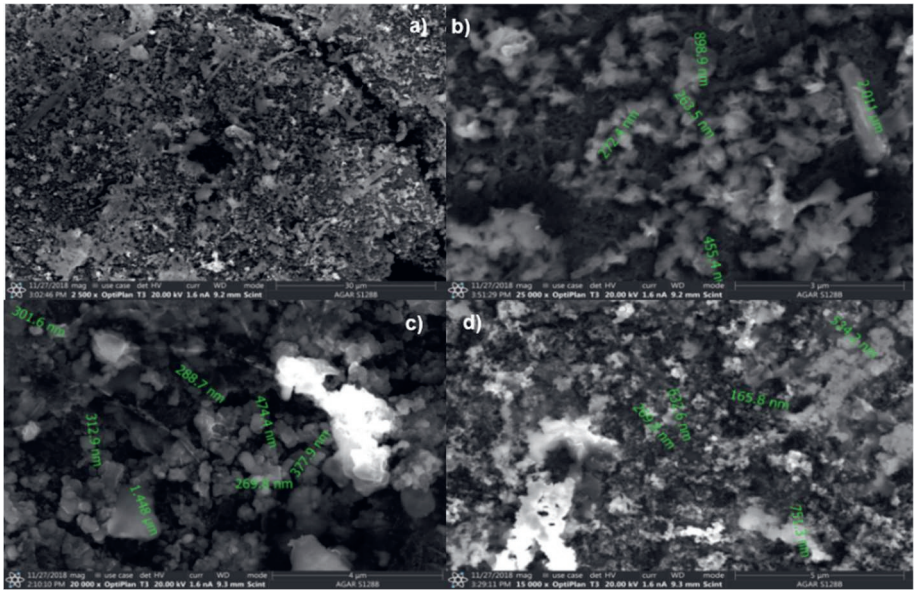

Figure A1. Catalyst morphology and distribution on GDEs a) overview of Pb catalyst: rods and irregular particles are predominant b) zoom-in on Pb catalyst c) Sn catalyst on GDE, consisting mostly of irregularly shaped particles d) Sn50Pb50 catalyst on GDE, similar to Sn only one.

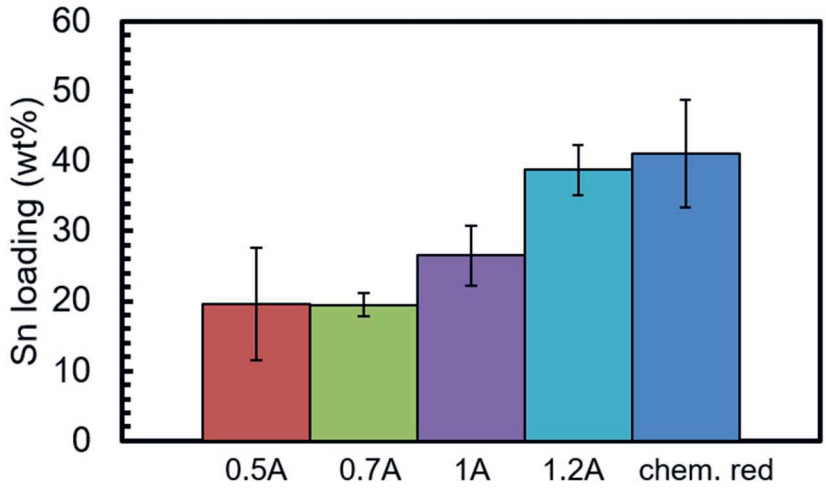

Figure A2. Sn loading on the carbon support estimated from EDX analysis.

Disintegration current	Charge passed	Weight loss	Max theoretical FY
1250 mA/cm^2	108C	13.7 mg	41.2%
1875 mA/cm^2	108C	20.47mg	61.6%
2500 mA/cm^2	108C	38.81mg	116.8%

Table A1. Weight loss of Sn wires in 0.1M NaOH at different currents but same charge passed. The maximum theoretical FY is calculated for a 4-electron transfer reaction (discussed below). Since it is hard to separate electrochemical and eventual mechanical contributions to disintegration, this value may be significantly lower. Nonetheless, a trend of increasing yield at higher current density when the charge is fixed is evident.

Catalyst	Starting V	Starting power	Reaction time
Sn/C 0.5A (1042 mA/cm^2)	15.5 V	7.75 W	16 min
Sn/C 0.7A (1458 mA/cm^2)	19 V	13.3 W	10.5 min
Sn/C 1A (2083 mA/cm^2)	20.5 V	20.5 W	8 min
Sn/C 1.2A (2500 mA/cm^2)	20.5 V	24.6 W	6.5 min

Table A2. Summary of reaction conditions for the cathodic disintegration synthesis. The current densities are calculated on the basis of the 0.48 cm^2 area of wire exposed to the electrolyte. This current density is only valid with the starting geometry of the wire, which is going to change during corrosion. The starting V of Sn/C 1A and Sn/C 1.2A is the same (maximum V reachable by the power supply). This was achieved by reducing the distance between anode and cathode and therefore the ohmic drop between the two.

A.2 Calculation of atom efficiency of the synthesis. The atom efficiency is a useful indicator, commonly used in organic synthesis, which describes how many of the atoms present in the reagents can be found in the product. Any atom or molecule remaining in the reaction mixture which is not a desired product is waste and needs to be disposed of. The atom efficiency can be calculated from the stoichiometrically balanced chemical reaction. To calculate the atom efficiency we utilized the following chemical reactions.

CHEMICAL REDUCTION:

$$SnCl_2 + 2\ NaBH_4 + 6\ H_2O \longrightarrow Sn + 2\ NaCl + 2\ B(OH)_3 + 7\ H_2 \quad (A1)$$

In this case, we assumed that water would take part in the reaction since the ethylene glycol used for the synthesis was

not anhydrous and the Sn salt contained water being in dihydrate form.

In the case of the cathodic disintegration we are assuming that the production of metallic particles goes through the formation and immediate oxidation by the aqueous electrolyte (with production of hydrogen) of unstable Zintl phases. We calculated the atom efficiency basing the calculation on two possible cluster anion candidates: the most well documented one (Sn_9^{4-}) and the one that was most unfavorable for our calculation (i.e. with the worst negative charge to number of Sn atoms in the cluster ratio, being Sn_4^{4-}).

CATHODIC DISINTEGRATION:

Cathode half-reaction

$$9(4)\ Sn + 4e^- + 4\ Na^+ \longrightarrow Na_4Sn_{9(4)} + 4\ H_2O \longrightarrow Sn_{9(4)} + 4\ Na^+ + 4\ OH^- + 2\ H_2 \quad (A2)$$

Anode half-reaction

$$4\ OH^- \longrightarrow O_2 + 4\ e^- + 2\ H_2O \quad (A3)$$

Overall reaction

$$9(4)\ Sn + 2\ H_2O \longrightarrow Sn_{9(4)} + 2\ H_2 + O_2 \quad (A4)$$

For all the reactions it is left implicit the subsequent agglomeration of the Sn atoms or clusters into larger particles. In the case of the particles produced with disintegration we are also assuming that the clusters are oxidized by the water and coalesce into particles before being captured by the carbon.

Using the formula for the atom efficiency = $\frac{\Sigma\ \text{MW desired products}}{\Sigma\ \text{MW all reagents}} * 100$ (A5)

we get a value of 31.8% for the chemical reduction route, 96.7% for the cathodic disintegration considering the Zintl phase based on Sn_9^{4-} and 92.9% considering the Zintl phase based on Sn_4^{4-}.

Appendix B

Supporting Information to Chapter 4: Cathodic disintegration of Sn and Pb: some evidence for a Zintl phase mediated mechanism and possible implications for electrocatalysis

B.1 Supplementary Figures

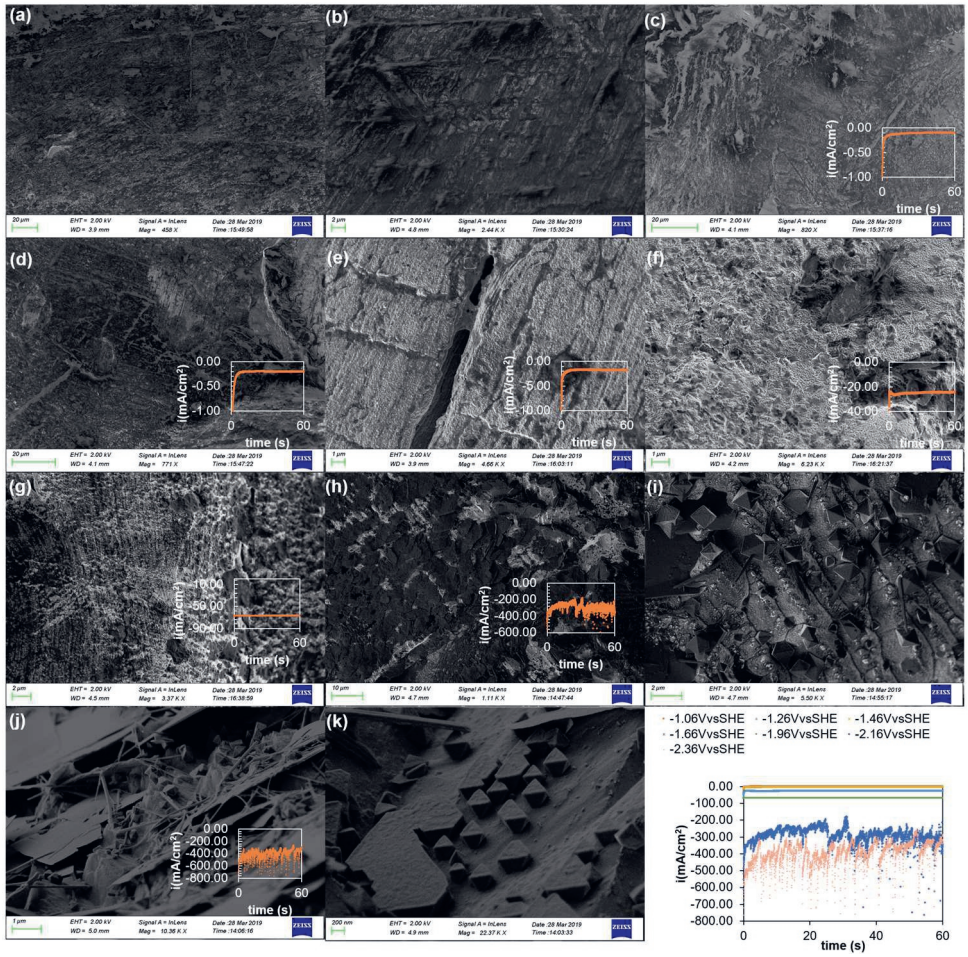

Figure B1. Polarization sequence of Pb in 1M NaOH. (a) photograph of a pristine (not exposed to the electrolyte) and (b) blank (exposed to the electrolyte for 60 seconds but not polarized). (c) -1.06 vs SHE (d) -1.26 vs SHE (e) -1.46 vs SHE (f) -1.66 vs SHE (g) -1.96 vs SHE (h) -2.16V vs SHE (visible disintegration starts) - Sheets (i) -2.16V vs SHE –Octahedral structures and rods (j) -2.36V vs SHE – close up on debris (rods and sheets) showing some octahedral structures below (k) -2.36V vs SHE – close up on octahedral decomposition. The current recorded during the 60-second runs are reported in the pictures and also summarized in the bottom right. For some potentials, where the process is more heterogeneous, more than a representative picture is shown.

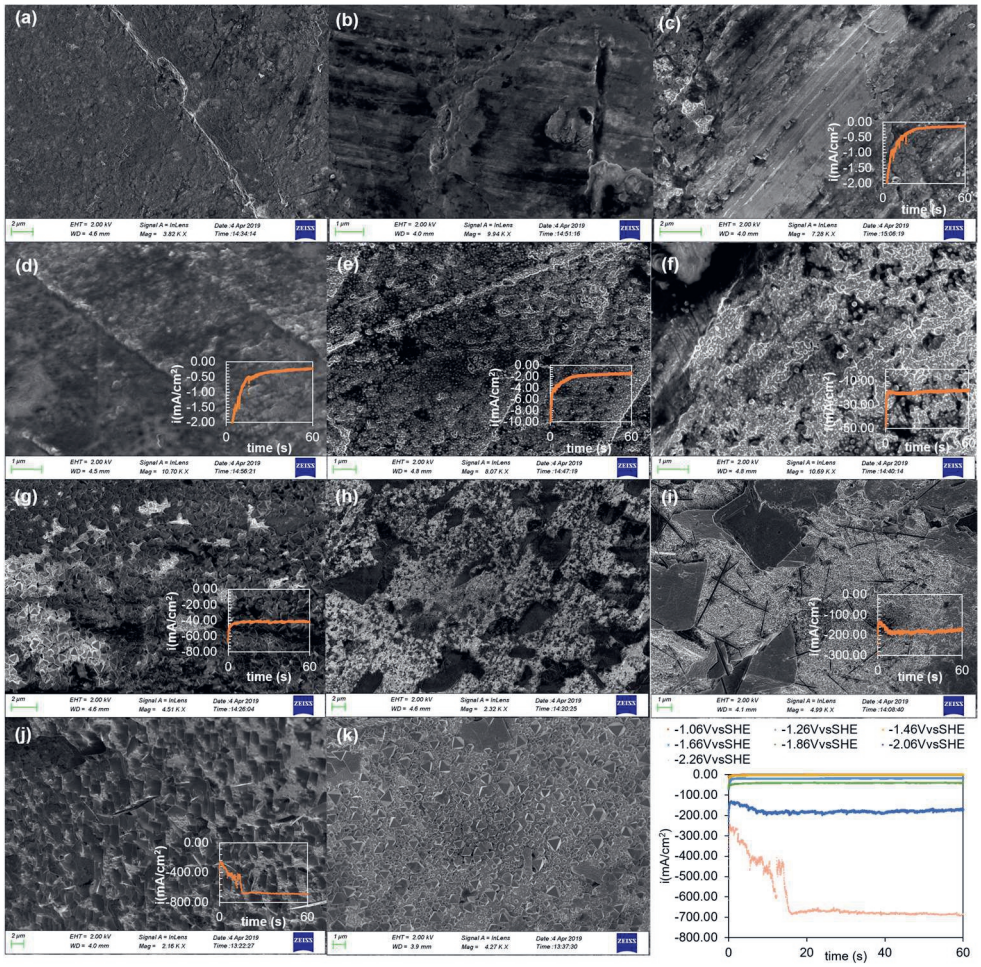

Figure B2. Polarization sequence of Pb in 0.5M Na_2SO_4. (a) photograph of a pristine (not exposed to the electrolyte) and (b) blank (exposed to the electrolyte for 60 seconds but not polarized). (c) -1.06 vs SHE (d) -1.26 vs SHE (e) -1.46 vs SHE (f) -1.66 vs SHE (g) -1.86 vs SHE – Roughening and first signs of octahedral decomposition (h) -1.86 vs SHE – Roughening and sheets (i) -2.06 vs SHE – Roughening, sheets and rods (j) -2.26 vs SHE (visible disintegration) – Sheets (k) -2.26 vs SHE – Octahedral patch.

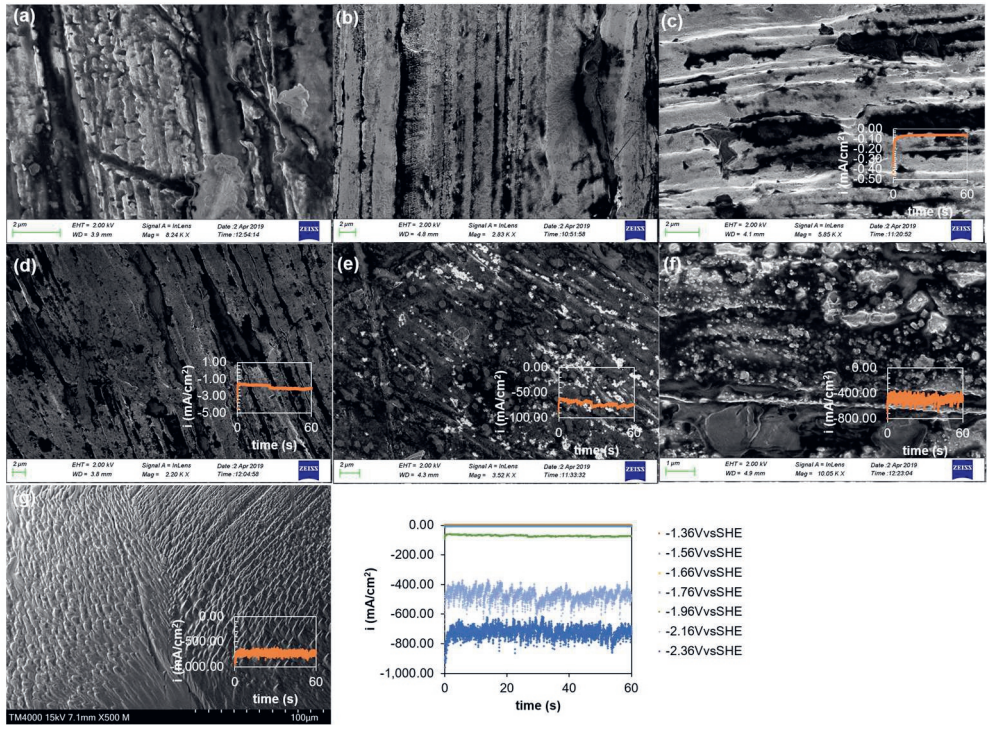

Figure B3. Polarization sequence of Sn in 1M NaOH. (a) photograph of a pristine (not exposed to the electrolyte) and (b) blank (exposed to the electrolyte for 60 seconds but not polarized). (c) -1.36 vs SHE (d) -1.66 vs SHE (e) -1.96V vs SHE – First evident signs of roughening (f) -2.16V vs SHE – roughening (g) -2.36V vs SHE (visible disintegration)– different disintegration patterns

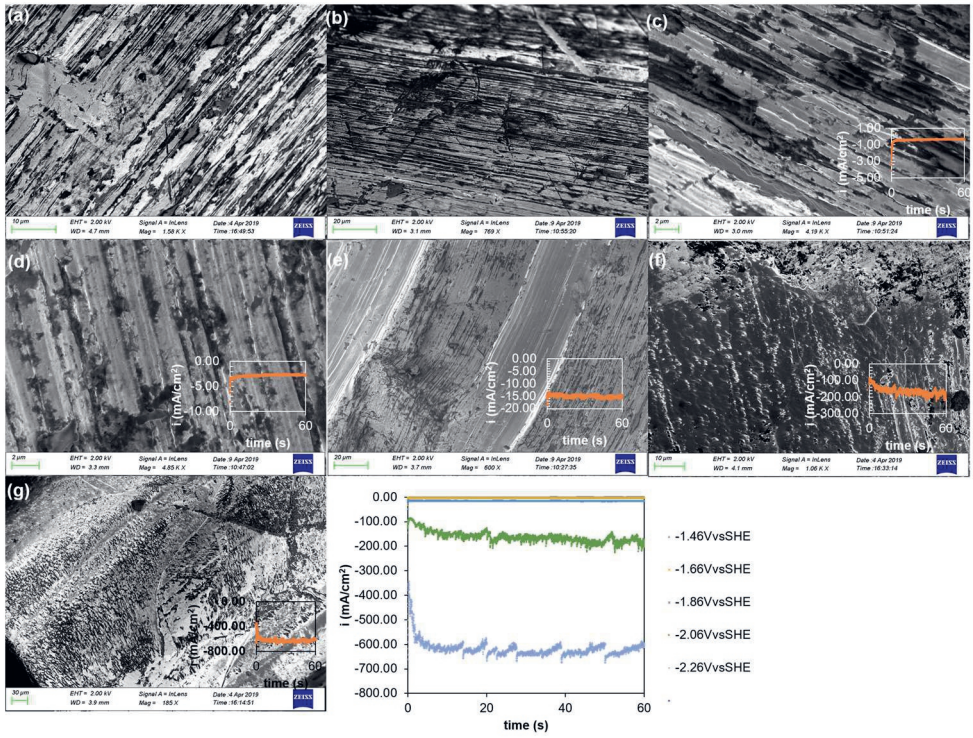

Figure B4. Polarization sequence of Sn in 0.5M Na_2SO_4. (a) photograph of a pristine (not exposed to the electrolyte) and (b) blank (exposed to the electrolyte for 60 seconds but not polarized). (c) -1.46 vs SHE (d) -1.66 vs SHE (e) -1.86V vs SHE (f) -2.06V vs SHE – Blistering and roughening (g) -2.26V vs SHE (visible disintegration) – Different etching features

Figure B5. (left) Photograph of a cathodically polarized Sn wire (in 0.1M NaOH) at the onset of visible disintegration, when the reaction is still slow and the surface of the wire is not completely surrounded by a cloud of disintegration products (visible behind the wire). Notice the golden halo surrounding the wire as well as the large amount of bubbles formed on the surface. (right) The same wire after polarization, showing the usual gray-metallic color of Sn. Notice the patchy pattern produced after disintegration.

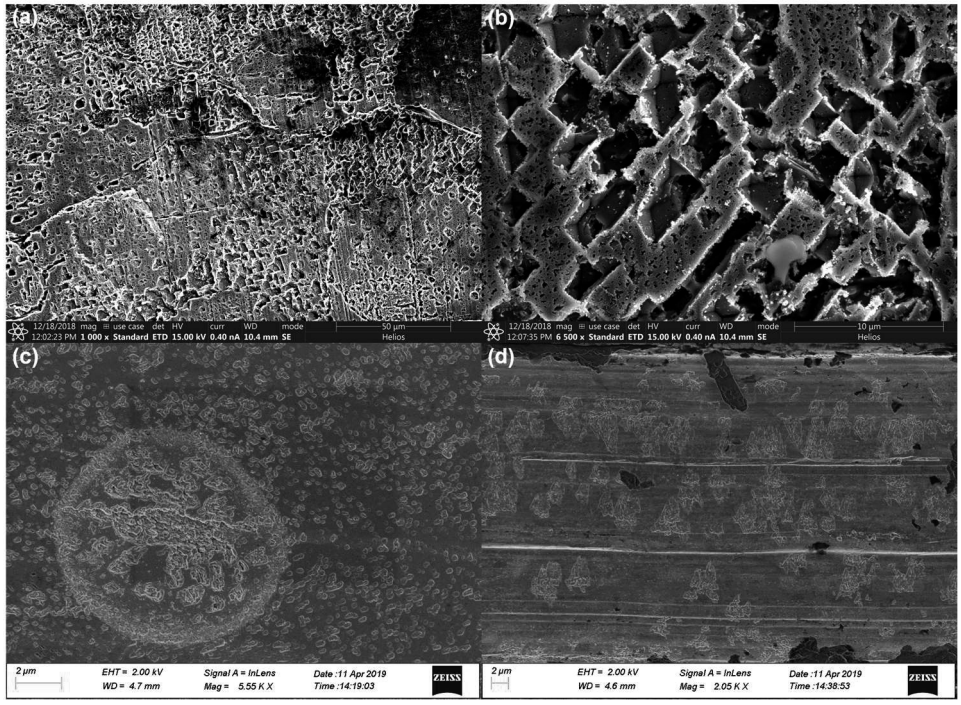

Figure B6. Etching patterns after cathodic polarization on Sn. (a)-(b) corrosion pattern after polarization in H_2SO_4 for several minutes with a power supply. (c)-(d) peculiar etching patterns on Sn polarized in 1M $NaNO_3$ for 60 seconds. During polarization in these electrolytes, macroscopic disintegration is not attainable, at least in the limits of our electrochemical equipment.

Appendix C

Supporting Information to Chapter 5: CO_2 electroreduction on bimetallic Pd-In nanoparticles

C.1 Supplementary Figures and Tables

Electrode	Composition (at%) from SEM-EDX		Metal loading on electrode (mg/cm^2)
	In	Pd	
In	100	0	0.16
$In_{95}Pd_5$	96.7 ± 1.7	3.3 ± 1.7	0.19
$In_{75}Pd_{25}$	77.7 ± 3.1	22.3 ± 3.1	0.16
$In_{50}Pd_{50}$	53.1 ± 4.0	46.9 ± 4.0	0.11
Pd	0	100	0.12

Table C1. Actual elemental composition of the catalysts and metal loadings on carbon cloth.

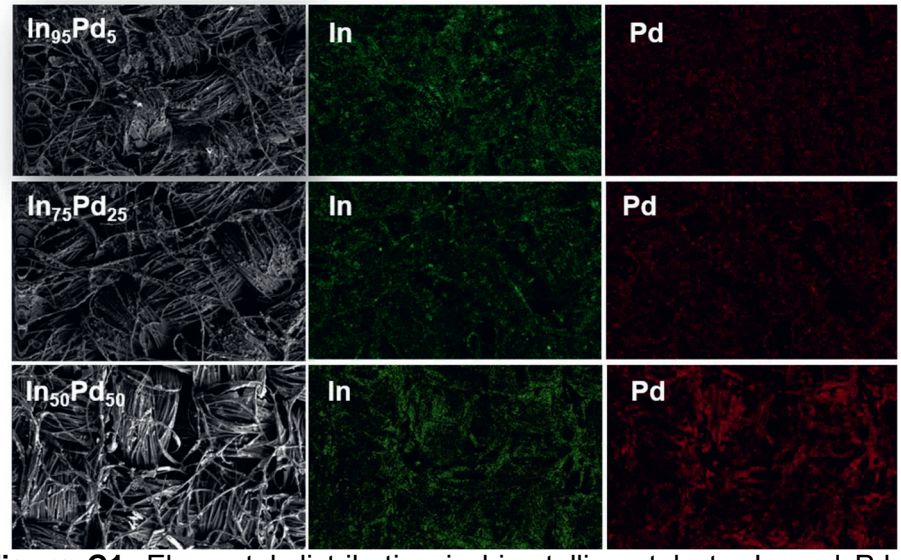

Figure C1. Elemental distribution in bimetallic catalysts. In and Pd are homogeneously dispersed on the carbon cloth.

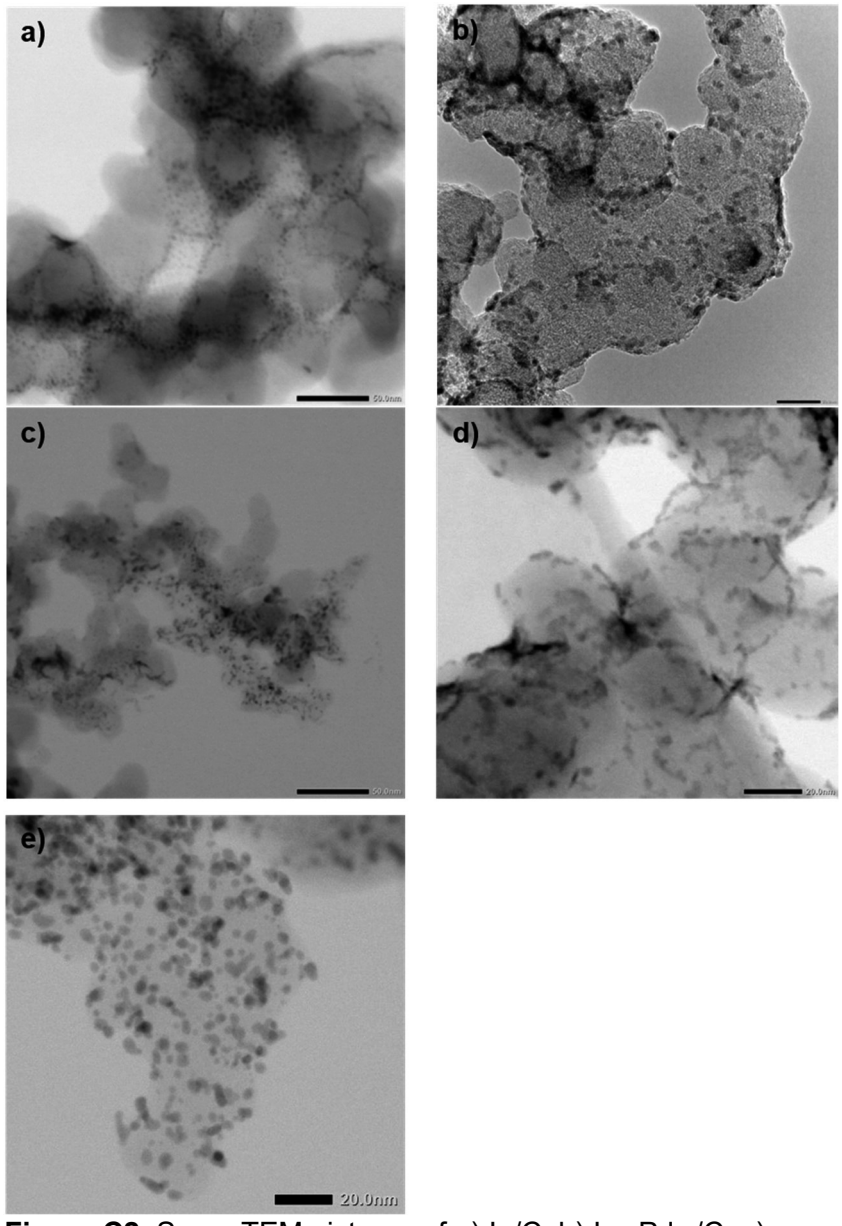

Figure C2. Some TEM pictures of a) In/C, b) $In_{50}Pd_{50}$/C, c) $In_{75}Pd_{25}$/C, d) $In_{95}Pd_{5}$/C and e) Pd/C nanoparticles. (Scale bar a), c) = 50 nm; scale bar b), d), e) = 20 nm)

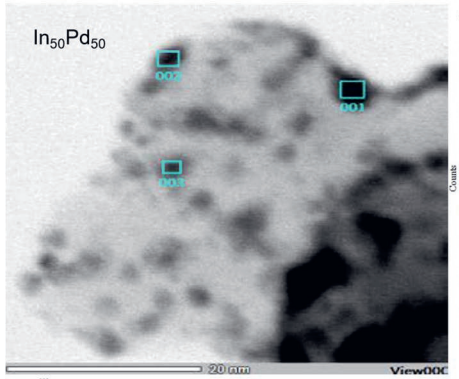
$In_{50}Pd_{50}$
002
001
003
20 nm

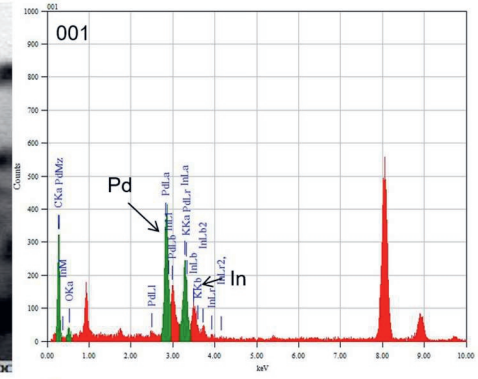
001
Pd
In
Counts
keV

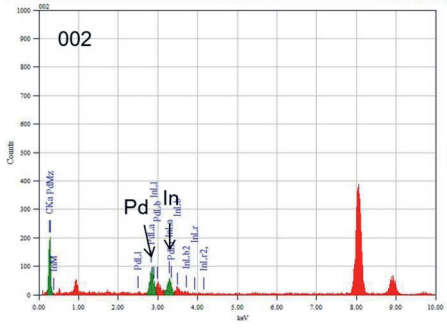
002
Pd
In
Counts
keV

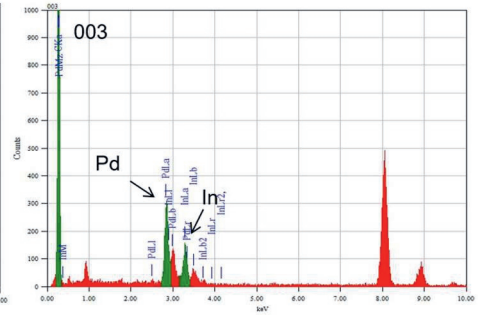
003
Pd
In
Counts
keV

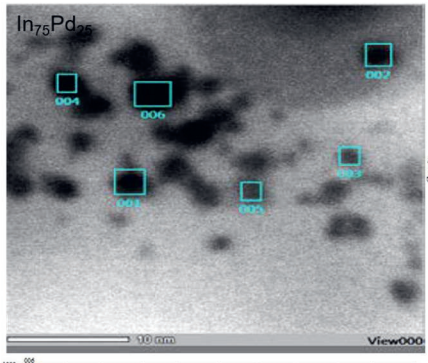
$In_{75}Pd_{25}$
004
006
002
001
005
003
10 nm

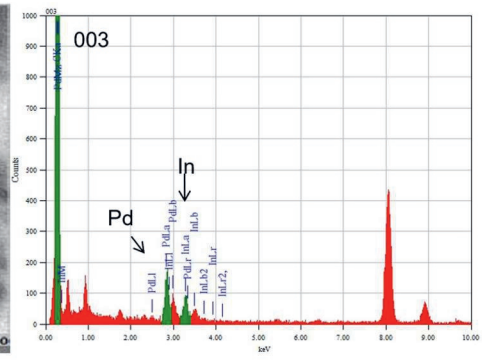
003
In
Pd
Counts
keV

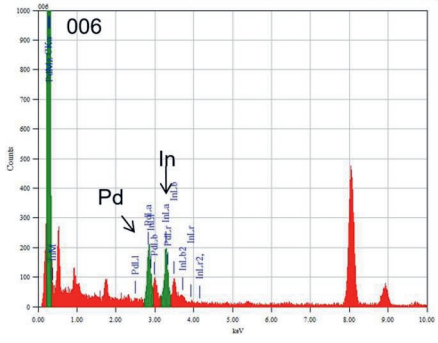
006
In
Pd
Counts
keV

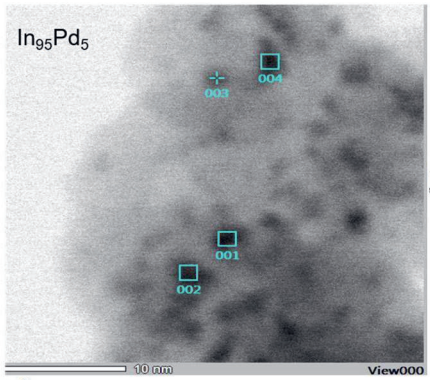
$In_{95}Pd_5$
004
003
001
002
10 nm
View000

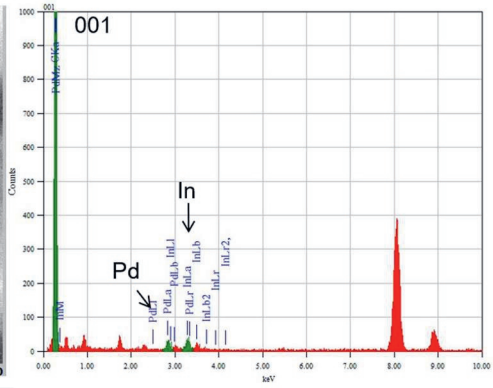
001
In
Pd
Counts
keV

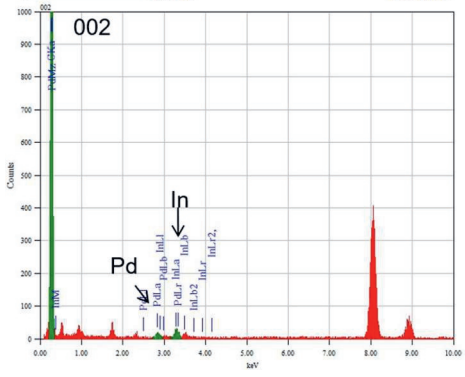
002
In
Pd
Counts
keV

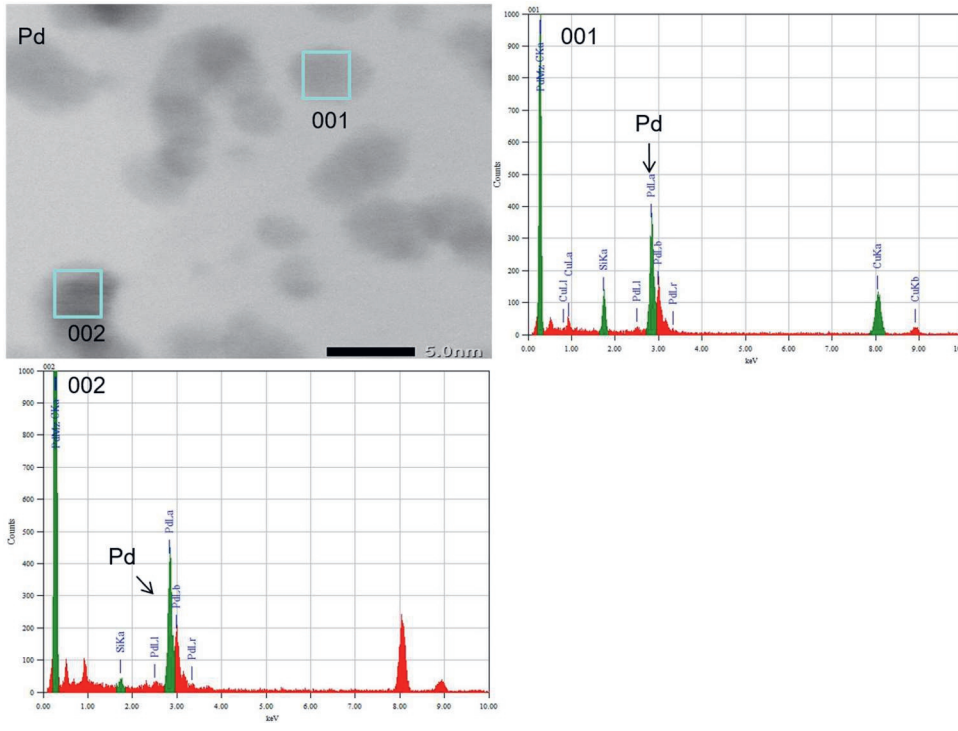

Figure C3. STEM-EDX spectra of some selected nanoparticles of different catalysts.

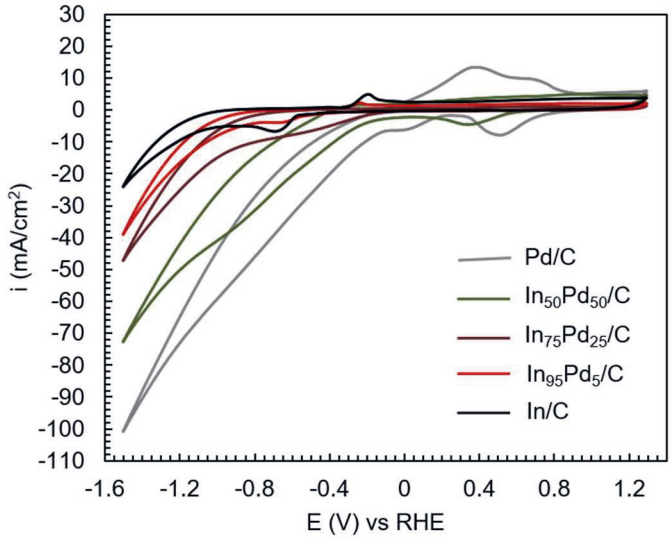

Figure C4. Cyclic voltammetries of the 5 catalysts in N_2 saturated 0.5M $KHCO_3$. Notice how the onset potential of HER shifts positively and results in higher currents. Also, the shape of the CVs, especially in $In_{50}Pd_{50}/C$ and $In_{75}Pd_{25}/C$ is dramatically changed and doesn't show characteristic peaks of either In or Pd.

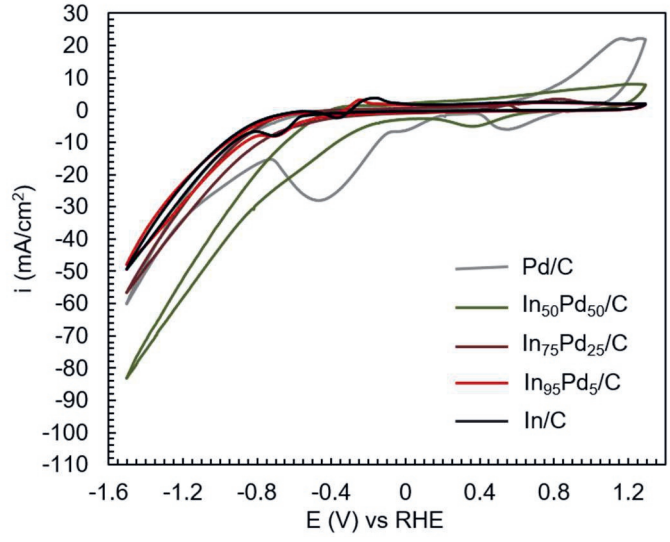

Figure C5. Cyclic voltammetries of the 5 catalysts in CO_2 saturated $KHCO_3$.

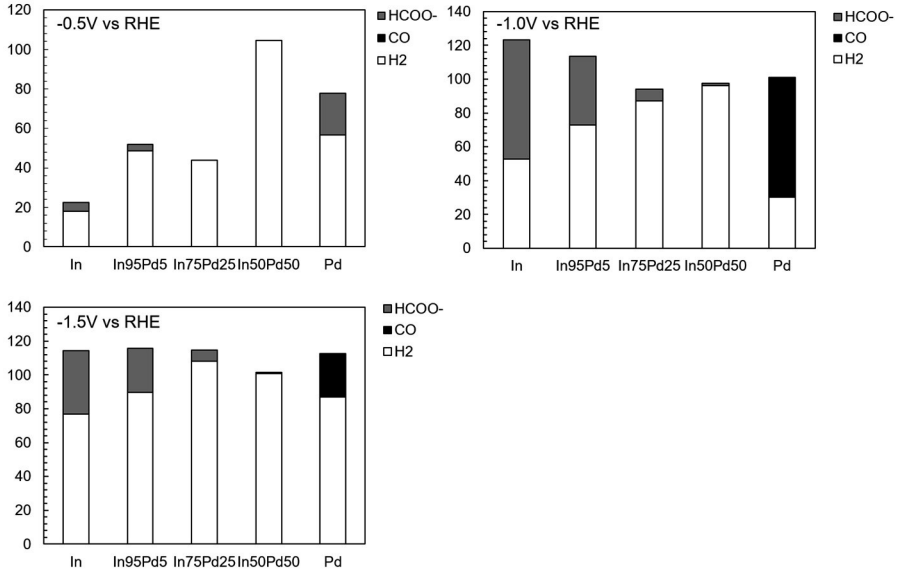

Figure C6. FY to gaseous products on the 5 catalysts. Considering the contribution from formate to the FY (main manuscript) Pd at -0.5V gives FY lower than 100%, this is likely due to the absorption of H in the Pd lattice as well as the formation of tightly bound CO which is not released or is released and below the detection limit of the GC due to the low overall currents achieved. In, $In_{95}Pd_5$ and $In_{75}Pd_{25}$ at -0.5V also give FY significantly lower than 100%, this could be due to part of the charge reducing oxides formed during air exposure. Always considering the formate contribution illustrated in the main manuscript: some runs give FY slightly above 100%. This is expected since different analytical methods are used for the detection of the products. Also, since during gas detection the system had to be sealed, the data for liquid-phase and gas-phase products come from different experiments.

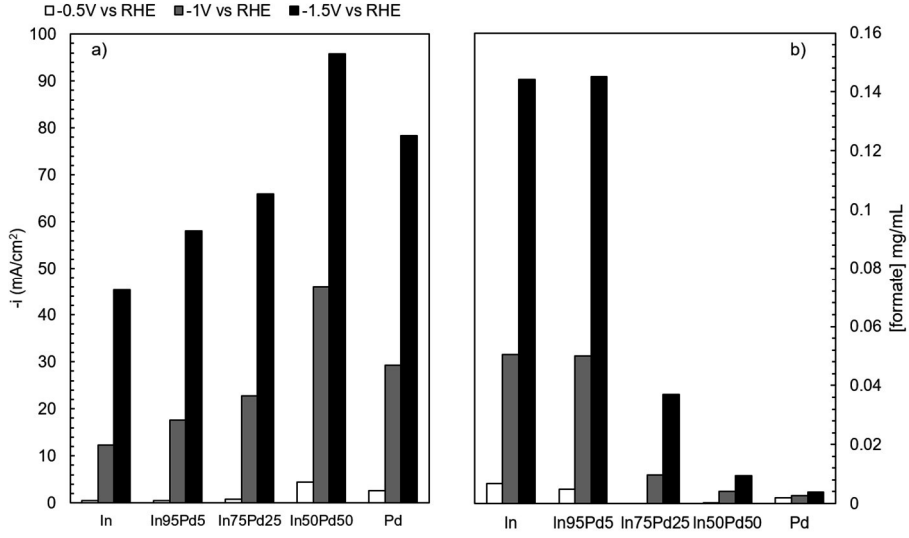

Figure C7. a) Current densities during the bulk electrolysis at the different potentials on all the catalysts. b) Concentrations of formate in mg/mL at the end of every 30-minute potential step for all the catalysts. In $In_{95}Pd_5$ the productivity of formate is the same as pure In, but the current is higher, resulting in a lower faradaic yield (see Figure 4 in the main manuscript).

Appendix D

Supporting Information to Chapter 6: Modulation of the selectivity of CO_2 to CO electroreduction in Palladium rich Palladium-Indium nanoparticles

D.1 Computational Details

D.1.1 Stability of the Pd_xIn_y systems. Initially, we performed structural optimization of Pd, In, the intermetallics PdIn, Pd_2In, Pd_3In, and solid solutions of In in Pd of approximate composition $Pd_{98}In_2$ and $Pd_{90}In_{10}$ (at.%). The crystal structures for the intermetallic compounds were retrieved from literature.[1,2,3,4] Models from solid Pd-In solutions were generated taking as base the Pd fcc conventional cell. The $Pd_{98}In_2$ composition was modelled from the 2×2×3 expansions of bulk Pd, containing 48 atoms, and replacing one of them by In. The $Pd_{90}In_{10}$ composition was modeled from the 2×2×2 expansion, containing 32 atoms, and replacing three non-adjacent Pd atoms by In. This allowed to find the correct lattice parameter and calculate the enthalphy of formation (ΔH_f) of the intermetallic compounds and solid solutions according to Equation D1. E_{Pd+In} is the energy calculated for the Pd_xIn_y bulk cell *via* density functional theory (DFT), N_{Pd+In} is the total number of atoms in the cell, N_{In} and N_{Pd} are, respectively, the number of In and Pd atoms in the cell, E_{In} and E_{Pd} are, respectively, the DFT energies of an In or Pd atom in their bulk structures.

$$\Delta \boldsymbol{H_f} = \frac{\boldsymbol{E_{Pd+In}}}{\boldsymbol{N_{Pd+In}}} - \frac{\boldsymbol{N_{In}}}{\boldsymbol{N_{Pd+In}}} * \boldsymbol{E_{In}} - \frac{\boldsymbol{N_{Pd}}}{\boldsymbol{N_{Pd+In}}} * \boldsymbol{E_{Pd}} \quad \textbf{(D1)}$$

The values obtained are summarized in Table D3 and compared to experimental values of solid solutions of similar compositions and intermetallic compounds.[1] Overall, DFT calculated formation energies are comparable with experimental enthalpies, even though they present a systematic offset of about 20%. The formation of Pd-In solid solutions and intermetallic compounds is thermodynamically favorable and the compounds are stable.

Given the very different surface energies of In and Pd (0.29 J m^{-2} for In(001) vs. 1.37 J m^{-2} for Pd(111), lowest energy termination for these metals) and the much larger thermodynamic drive for In to be oxidized, upon air exposure In could possibly migrate to the nanoparticles surface and segregate. However, our experimental results suggest otherwise. The XRD of $Pd_{98}In_2$/C and $Pd_{90}In_{10}$/C (Fig. 3) suggests that In is still incorporated in the Pd lattice, at least partially and the XPS

analysis confirms that indium is in its metallic state in these two catalysts (Fig. D5). Moreover, the separation and surface segregation of In, at least in the more In-rich $Pd_{50}In_{50}$/C, could result in a relatively thick In surface layer which should be detectable in the cyclic voltammetry. On the contrary, the cyclic voltammogram of $Pd_{50}In_{50}$/C (Fig. 2) presents a distinct shape, not traceable to either Pd or In, suggesting that intermetallic compounds with a different structure, stoichiometry and electronic properties are stable on the surface. The exothermicity of the Pd-In bonds seems to be enough to stabilize the structures against segregation. Besides, whatever the behavior of the bimetallic systems may be upon air exposure, the reducing conditions imposed during electrolysis could change the situation drastically, as the potentials investigated in this study are well below the redox potentials of In and Pd.

To check whether solid solutions of In in Pd would be stable against a competing ordered intermetallic phase we calculated enthalpies for the demixing of the solid solutions (s.s.) into pure Pd + Pd-In intermetallics (Fig. D7). Demixing enthalpies were calculated according to the stoichiometry of the following reactions, Equations D2-D7:

$$\mathbf{Pd_{29}In_3(s.s.) \rightarrow Pd_{26} + 3PdIn} \quad \textbf{(D2)}$$

$$\mathbf{Pd_{29}In_3(s.s.) \rightarrow Pd_{23} + 3Pd_2In} \quad \textbf{(D3)}$$

$$\mathbf{Pd_{29}In_3(s.s.) \rightarrow Pd_{20} + 3Pd_3In} \quad \textbf{(D4)}$$

$$\mathbf{Pd_{47}In_1(s.s.) \rightarrow Pd_{46} + PdIn} \quad \textbf{(D5)}$$

$$\mathbf{Pd_{47}In_1(s.s.) \rightarrow Pd_{45} + Pd_2In} \quad \textbf{(D6)}$$

$$\mathbf{Pd_{47}In_1(s.s.) \rightarrow Pd_{44} + Pd_3In} \quad \textbf{(D7)}$$

The only thermodynamically favorable process is the demixing of In-Pd solid solution into pure Pd and ordered Pd_3In. For $Pd_{47}In$ this

reaction is only slightly exothermic (–0.08 eV / atom), whilst for increased indium content, $Pd_{29}In_3$, there is a significant thermodynamic drive for the decomposition of the solid solution (–0.24 eV / atom). This is in line with the Pd-In phase diagram. The formation of solid solutions or intermetallic compounds are competing processes and the formation of intermetallic compounds becomes dominant beyond a certain In concentration.

The stability of the Pd-In solid solutions against segregation and islanding of In atoms was investigated according to a systematic approach previously applied.[5] We modelled 4-layers, 64 atoms Pd(111) slabs with the topmost two layers allowed to relax, with 1 or more In substituents in different arrangements. This allowed to estimate the tendency of In to segregate on the surface and to form islands as opposed to being isolated and surrounded by Pd atoms. The results are reported in Fig. D8 and suggest that In atoms in the Pd matrix have a slight tendency to be on the surface (even before accounting for the larger oxygen affinity of In), rather than being in the bulk or forming near surface alloys (NSA). Also, In prefers being surrounded by Pd atoms, rather than forming islands.

D.1.2 Adsorption of relevant intermediates. For the investigation of the catalytic properties of the synthesized nanoparticles, we initially determined the most stable surfaces of Pd, In and the intermetallic compounds by optimizing different surface terminations. The values of the surface energy for the investigated surfaces are reported in Table D5. Then, we assessed intermediates adsorption on the most stable surfaces, expected to be the most abundant facets on nanoparticles according to Wulff theorem.[6,7] For the Pd-In solid solution we used a Pd(111) slab with one In atom on the surface.

D.2 Attenuated Total Reflectance (ATR) Spectroscopy

D.2.1 Methodology. Fig. 4 in the main text shows the ATR spectra of the five catalysts in a gaseous atmosphere of CO (on the left) and after purging with Ar (right) to allow desorption of weakly adsorbed CO. Before adsorbing CO, the catalysts were pre-reduced in a pure H_2

atmosphere for 45 minutes. This reduction procedure is enough to reduce Pd oxide, since it can be reduced by hydrogen below room temperature even in dilute hydrogen streams,[8] but not to reduce oxidized In, which remains in its oxide form even under high temperature and hydrogen pressures.[9,10] Our XPS analysis of the In 3d orbitals (Fig. D5) shows that while pure In nanoparticles are fully oxidized, the In in $Pd_{98}In_2$/C and $Pd_{90}In_{10}$/C is fully metallic, indicating that incorporation in the Pd lattice can protect In atoms from oxidation. Thus, the reduction treatment should be effective also for these catalysts. The situation is more complicated for $Pd_{50}In_{50}$/C because the In peak in this catalyst roughly coincides with the one of In^{3+}. This could mean that the In in the particles is fully oxidized, but also that the interaction with Pd is dramatically altering its electronic structure. In any case, since during bulk electrolysis the $Pd_{50}In_{50}$/C does not behave like any of the parent metals, we conclude that even if In is fully oxidized before the reaction, it would alloy with Pd during reduction (or else, if a thick In shell would have remained during electrochemical reaction, the catalyst behavior should be similar to pure In both in CVs and electrolysis).

D.2.2 Band assignment. For palladium, infrared bands in the range of 2060-2100 cm^{-1} are normally assigned to linear-bound CO, while bands in the range between 1750-2000 cm^{-1} are assigned to bridged and multi-bonded CO.[11] The bands in the spectra in Fig. 4 are a convolution of hollow and bridge sites (more intense band) and top sites (less intense band) on the different adsorption sites present on the nanoparticles, such as terraces, steps, corners and defects. The slightly different adsorption energies on similar sites (for example a bridge bonded CO on a terrace or an edge), cause the broadening of the peaks.

Pd/C, $Pd_{98}In_2$/C and $Pd_{90}In_{10}$/C show very similar spectra. Specifically, Pd/C and $Pd_{98}In_2$/C behave very similarly both in CO atmosphere and after Ar stripping. There does not seem to be a significant peak shift, meaning that the average adsorption energy of CO is constant. In addition to this, the bands look qualitatively the same, indicating that

the binding mode is also analogous. Since the peaks here represent a convolution of several similar adsorption modes, it is difficult to highlight small alterations in the adsorption geometry. In order to identify possible differences, we integrated the “hollow + bridge” band and the “top” band and plotted the ratio “top”/”hollow+bridge” (Fig. D6). From this analysis we find that Pd/C and $Pd_{98}In_2$/C show the same ratios in both CO and Ar. $Pd_{90}In_{10}$/C instead has a significantly higher ratio of top sites in CO atmosphere. After stripping with Ar the spectrum becomes similar to the other two Pd-rich catalysts, indicating that $Pd_{90}In_{10}$ may possess some additional CO adsorption sites which bind the molecule more weakly and could be separate from the strong binding sites which cause surface poisoning. These strongly adsorbing sites could instead be analogous to the ones on the other two catalysts, suggesting that this material may be composed of patches of Pd-In solid solution (similar reactivity as $Pd_{98}In_2$/C and Pd/C) and intermetallic compounds with a different adsorption behavior. This would be in agreement with the Pd-In phase diagram, since the composition is beyond the solubility limit of In in Pd, thus enabling the formation of intermetallic compounds.

The CO adsorption behavior in the gas phase of $Pd_{50}In_{50}$/C is comparable with previously reported catalysts with similar composition. The formation of the intermetallic compound PdIn with a CsCl structure and fully isolated Pd atoms leads to exclusive adsorption of CO on top of the isolated Pd atoms.[12] In our case only a weak CO vibration is detected, which could be either a red-shifted on-top or a blue shifted bridge adsorption site. This suggests that intermetallic compounds presenting different surface reactivity may be formed, at least after the reducing treatment. In does not show any CO adsorption, as expected since In catalyst should be present as In oxide, and this element does not adsorb CO even in the metallic state.

D.3 Supplementary Tables

Catalyst	Composition (at.%)				Electrode metal loading (mg/cm^2)
	SEM-EDX		XPS		
	In	Pd	In	Pd	
In/C	100	0	100	0	0.16
$Pd_{50}In_{50}$/C	53.1 ± 4.9	46.9 ± 4.0	45.59	54.41	0.11
$Pd_{90}In_{10}$/C	10.5 ± 1.4	89.5 ± 1.4	10.01	89.99	0.14
$Pd_{98}In_2$/C	n.d.	100	2.97	97.03	0.13
Pd/C	0	100	0	100	0.12

Table D1. Atomic % composition of the catalysts from SEM-EDX and XPS. Estimated metal loading on the electrodes used in the study.

Catalyst	Particle size from TEM (nm)
In/C	3.6 ± 0.9
$Pd_{50}In_{50}$/C	3.7 ± 0.4
$Pd_{90}In_{10}$/C	3.8 ± 1.0
$Pd_{98}In_2$/C	4.1 ± 1.0
Pd/C	4.4 ± 1.2

Table D2. Average particle size from TEM pictures.

	ΔH_f (eV/atom)	
	This study	**Experimental**[13]
$Pd_{47}In$ (s.s.)	-0.04	-0.05
$Pd_{29}In_3$ (s.s.)	-0.17	-0.21
Pd_3In (IMC)	-0.47	-0.55
Pd_2In (IMC)	-0.52	-0.63
PdIn (IMC)	-0.51	-0.63

Table D3. Formation enthalpy of Pd-In solid solutions and intermetallic compounds. $Pd_{47}In$ and $Pd_{29}In_3$ are models of solid solutions (s.s.), while the remaining models are of Pd-In intermetallic phases (IMC). Beyond a certain In concentration, the systems will show a tendency to form intermetallic compounds rather than solid solutions, as expected from the Pd-In phase diagram.

Crystal structure	**Lattice parameters**
In: tetragonal	a = 3.25 Å; c=4.94 Å
Pd: fcc	a = 3.94 Å
PdIn: cubic	a = 3.31 Å
Pd_2In: orthorhombic	a = 4.24 Å; b = 5.72 Å; c = 8.39 Å
Pd_3In: tetragonal	a = 4.11 Å; c = 7.74 Å
Pd-In solid solution	$d_{Pd\text{-}In}$ = 3.97 Å

Table D4. Crystal structures and lattice parameters of the model crystals resulting from DFT calculations.

Surface	γ (J m^2)
In (001)	**0.28**
In (010)	0.36
In (100)	0.36
In (110)	0.39
In (111)	0.44
PdIn (100)	1.27
PdIn (110)	**0.72**
PdIn (111)-In-t	1.05
PdIn (111)	0.80
Pd_2In (010)	**1.17**
Pd_2In (110)	1.20
Pd_2In (111)	1.27
Pd_3In (100)	**1.31**
Pd_3In (110)	1.41
Pd_3In (110)-Pd-t	1.37
Pd (100)	1.55
Pd (110)	1.63
Pd (111)	**1.37**

Table D5. DFT-calculated surface energies for different facets of pure In and Pd and intermetallic compounds. The In-t and Pd-t denominations stand for a surface terminated with either In only or Pd only. The most stable surfaces are highlighted in bold.

Surface	Adsorbate	ΔE_{DFT} (eV) Sites		
		Top	Bridge	Hollow
Pd(111)	**H**			–0.69
	CO			–1.54
	COOH	–0.36		
Pd_3In(100)	**H**		+0.35 (Pd-Pd)	–0.66 (4Pd Pd_{ss}) –0.27 (4Pd In_{ss})
	CO	–0.77(Pd)	–1.10 (Pd-Pd)	–1.44 (4Pd Pd_{ss}) –0.98 (4Pd In_{ss})
	COOH	+0.52(In) –0.12(Pd)		
Pd_2In(010)	**H**			–0.48 (3Pd In_{ss})
	CO	–0.67(Pd)	–0.95 (Pd-Pd)	–0.96 (3Pd Pd_{ss}) –1.02 (3Pd In_{ss})
	COOH	+0.38 (In) –0.24 (Pd)		
PdIn(110)	**H**	+0.75 (In) +0.21(Pd)		+0.82(2In 2Pd Pd_{ss}) +0.08(2In 2Pd In_{ss})
	CO	+0.59 (In) +0.00 (Pd)		+0.63(2In 2Pd Pd_{ss}) +0.68(2In 2Pd In_{ss})
	COOH	+0.56 (In) +0.07(Pd)		
In(001)	**H**			+0.76
	CO		+0.52	
	COOH	+0.31		

Table D6. Binding energies for different adsorption configurations on the investigated intermetallic compounds, In and Pd. Specific adsorption sites are reported within brackets, whilst ss subscript stands for subsurface atom.

D.4 Supplementary Figures

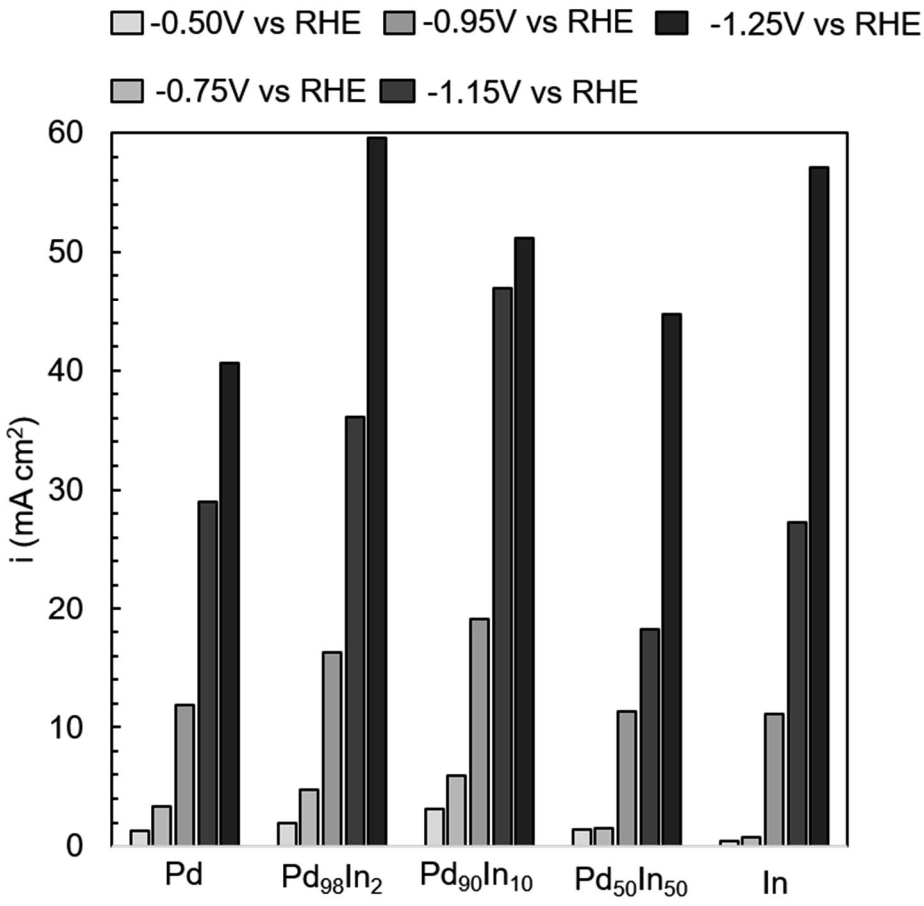

Figure D1. Average geometrical current densities recorded during bulk electrolysis. Progressively darker color indicates progressively more negative applied potential.

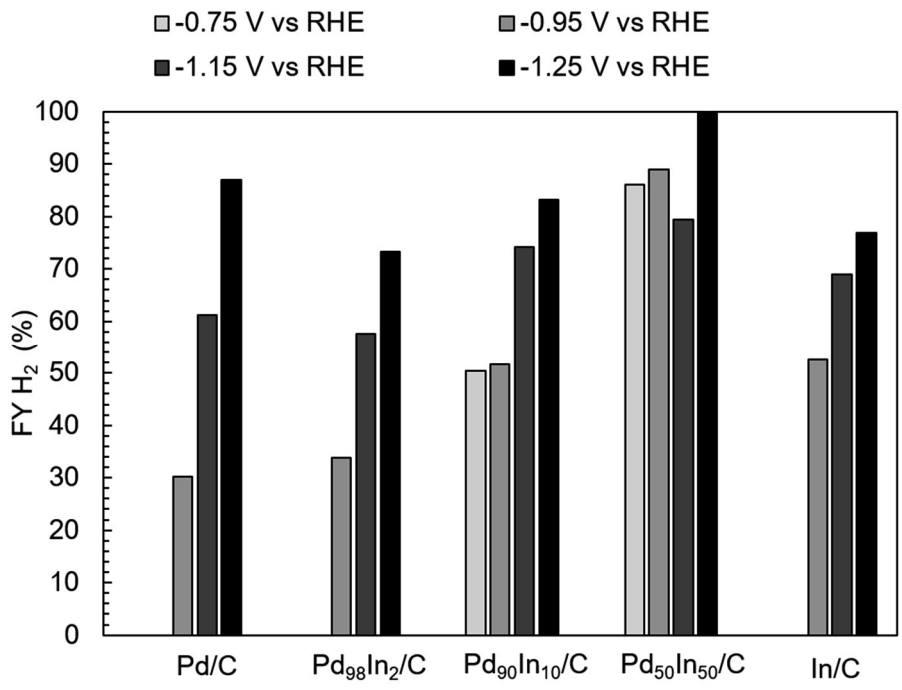

Figure D2. Faradaic yields towards hydrogen of the 5 catalysts. The value at –0.5V and in some cases at –0.75V could not be calculated due to small quantities of the gas being evolved, below the detection limit of the instrument. Due to possible interference of the He carrier gas in the H_2 peak, these values may be less accurate than the ones of CO.

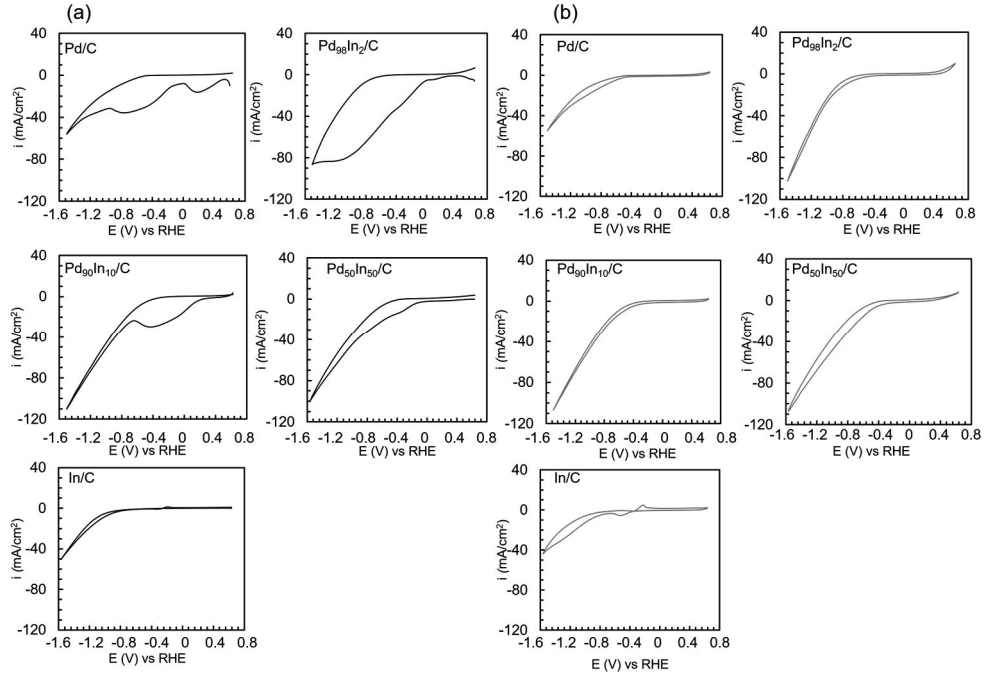

Figure D3. Voltammetric responses in 0.5 M $KHCO_3$, CO_2 saturated between –1.5V and +0.6 V to avoid CO re-oxidation: (a) first cycle, CO adsorption is visible; (b) from the second cycle the CVs do not show CO adsorption peaks, confirming the presence of surface sites susceptible to CO poisoning for Pd/C, $Pd_{98}In_2$/C and $Pd_{90}In_{10}$/C.

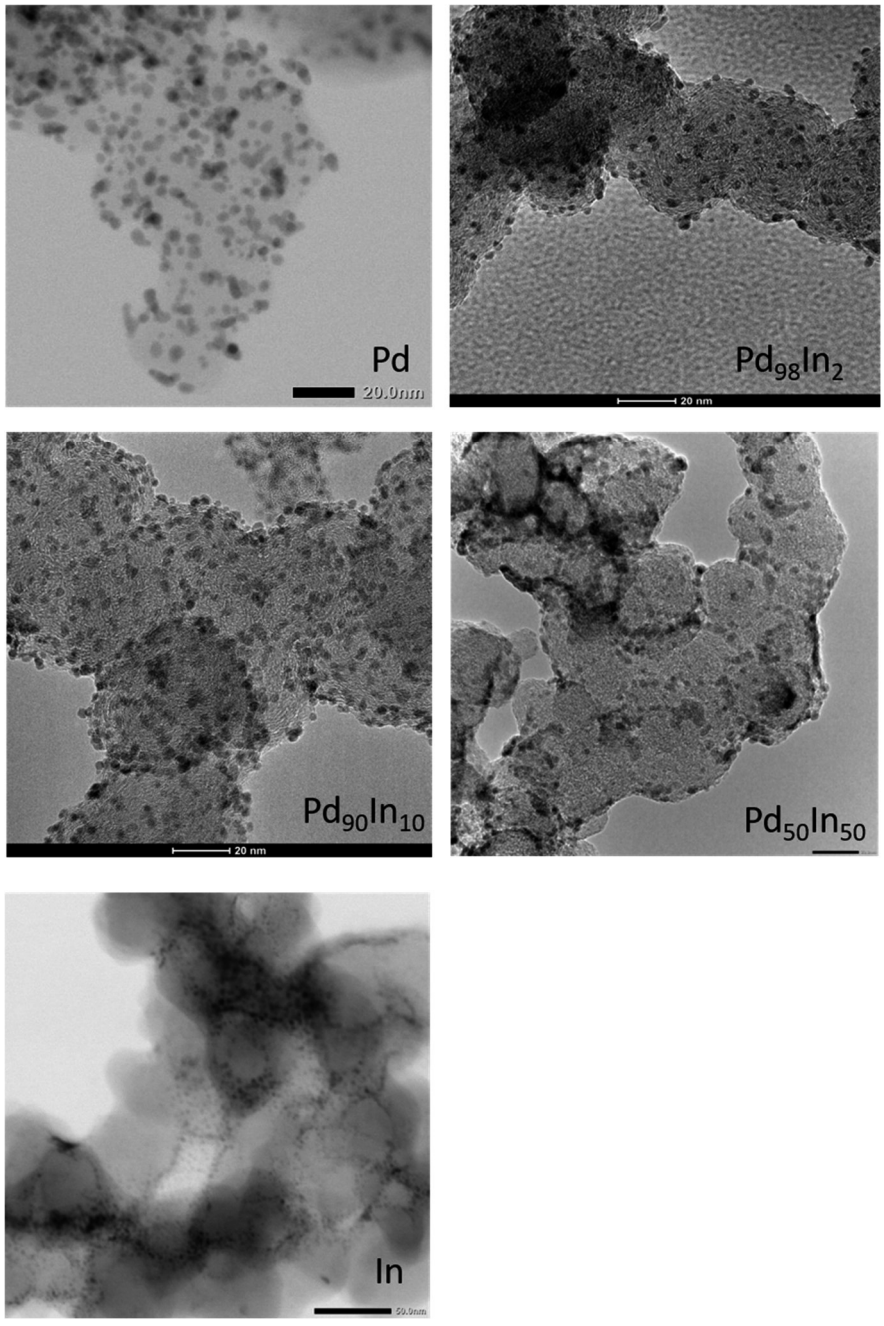

Figure D4. Representative TEM pictures of the investigated nanoparticles.

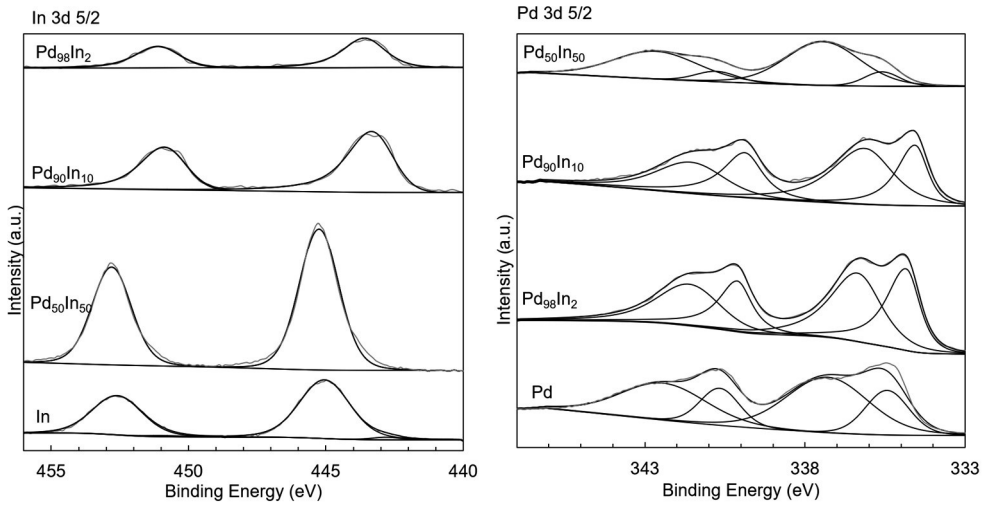

	In 3d 5/2	Pd^0 3d 5/2	Pd^{2+} 3d 5/2
In	445.33	–	–
$Pd_{50}In_{50}$	445.25	335.59	337.44
$Pd_{90}In_{10}$	443.34	334.57	336.13
$Pd_{98}In_2$	443.6	334.84	336.34
Pd	-	335.44	337.3

Figure D5. XPS spectra of the investigated catalysts. In 3d (left) and Pd 3d (right). Peak positions (maxima in eV) are summarized in the table.

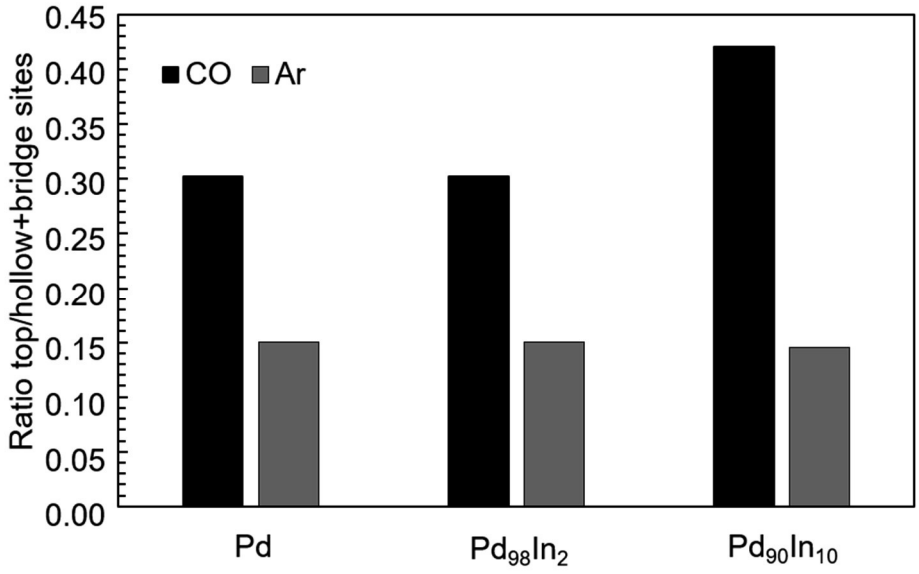

Figure D6. Ratio of the area of top sites divided by the area of hollow + bridge sites on the the Pd-rich catalysts in CO atmosphere (black bars, related to reversibly + irreversibly adsorbed CO) and after Ar stripping (gray bars, only irreversibly adsorbed CO), calculated from Fig. D3.

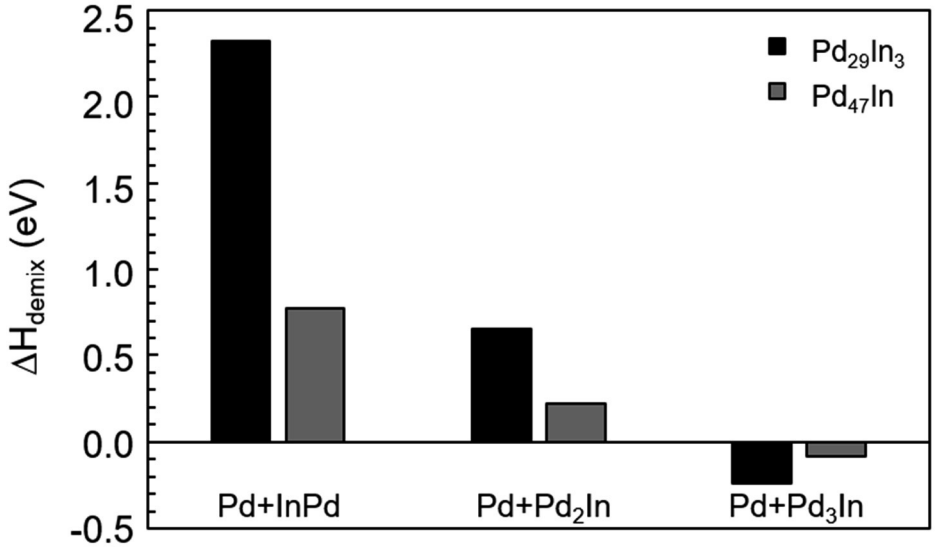

Figure D7. Enthalpies for the full demixing of solid solutions into pure Pd + ordered intermetallic phases.

Figure D8. Formation energy for different In substitution configurations in (4×4) Pd(111) vs energy of an analogous (4×4) Pd(111) slab normalized by the number of substitutions, N_{In}. Overall, In-Pd solid solutions present lower formation energies than pure Pd and In has a slight tendency to be isolated on the surface. Pd atoms are shown in gray, In atoms in purple. From left to right we have the following models: bulk In atom, In as near-surface-alloy (NSA), surface In atom, 2 surface In atoms separated by 2 Pd atoms, 2 adjacent surface In atoms, 2 NSA In atoms separated by 1 Pd atom, 2 adjacent NSA In atoms, 2 surface In atoms separated by 1 Pd atom, 1 surface In atom and 1 NSA In atom (non-adjacent), 1 surface In atom and 1 NSA In atom.

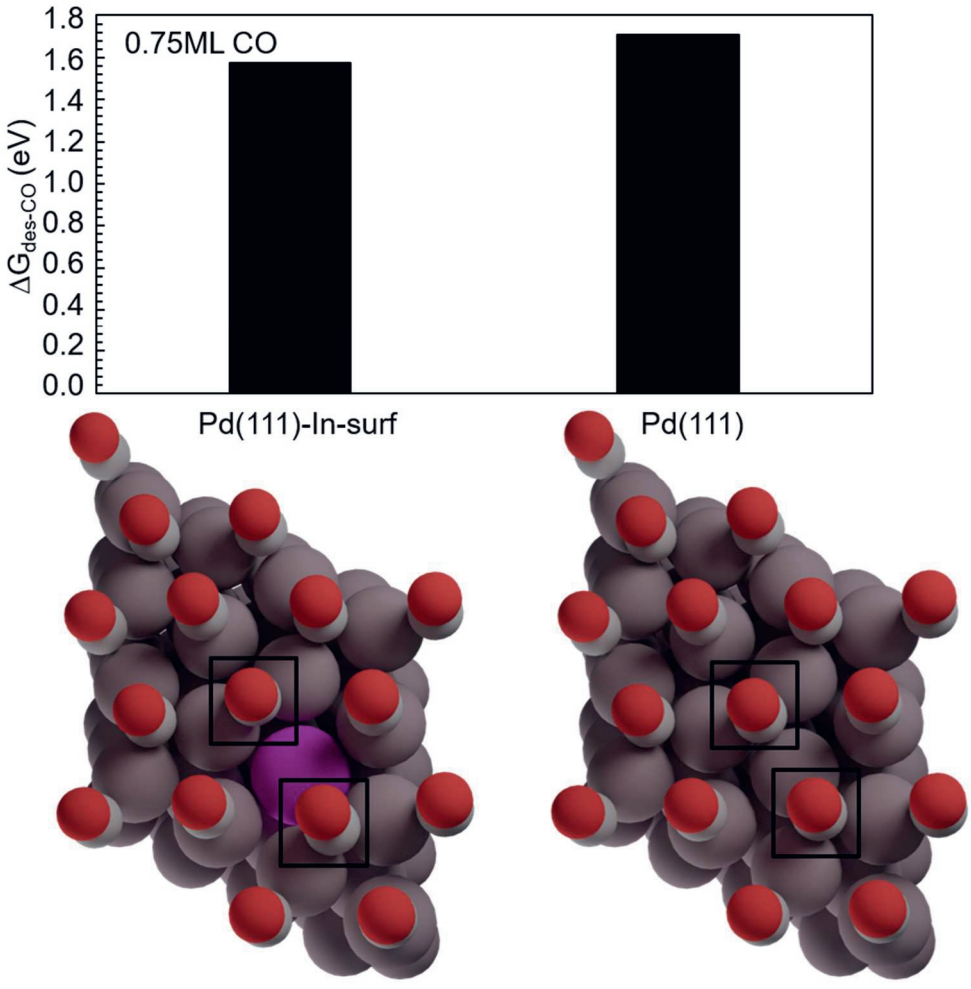

Figure D9. Average CO desorption energies at high CO coverage (0.75 ML) on Pd(111) and a Pd-In solid solution surface. Average binding energy and the binding mode does not change significantly between the systems. the two CO molecules close to the positively charged In substituent are repelled and pushed from a hollow to a bridge site on the Pd-In surface (see black squared insets). The differential CO desorption energy for the CO molecules in the frame is: +1.49 eV for the pure Pd system, +0.18 eV for the Pd-In system for a CO molecule on a 2Pd1In hollow site and +1.14 eV for CO molecule adsorbed on a bridge site, lowest energy configuration due to electrostatic repulsion on the Pd-In surface.

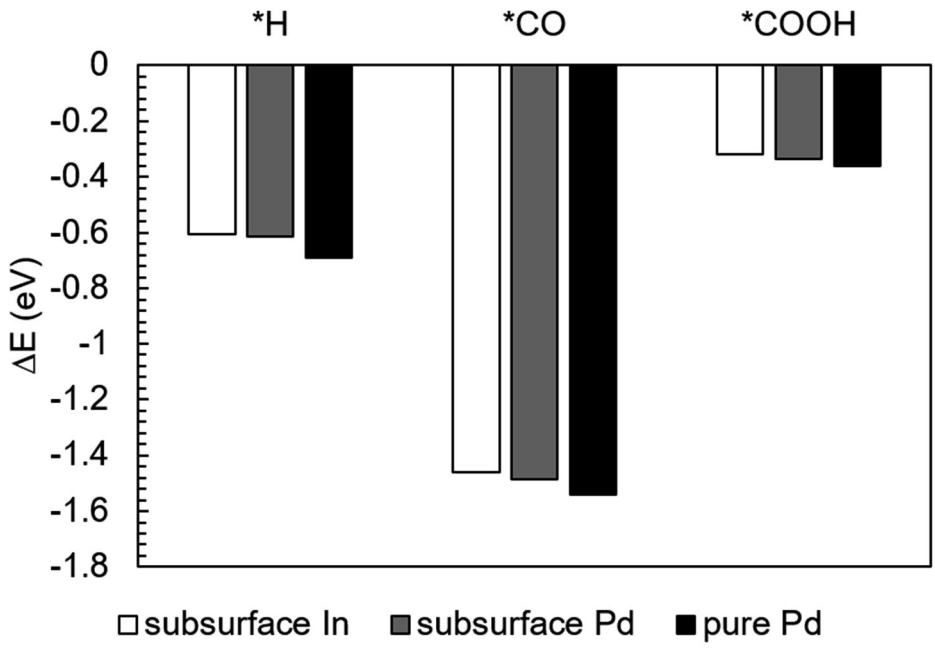

Figure D10. Adsorption energy of relevant intermediates on Pd surfaces. Indium atoms, if present, are in the subsurface. In white, binding energies when the adsorbate is placed in proximity of a subsurface In. In gray, binding energies when the adsorbate is placed far away from the subsurface In. In black, binding energies on a pure Pd slab. The adsorption properties of systems with subsurface In atoms do not change radically compared to pure Pd, since the Pd matrix screens electronic effects due to In. In affects surface reactivity only if present at the surface.

References

(1) Okamoto, H. In-Pd (Indium-Palladium). *J. Phase Equilibria*, 2003, 24, 481.

(2) Kohlmann, H. & Ritter, C. Reaction Pathways in the Formation of Intermetallic $InPd_3$ Polymorphs. *Zeitschrift für Anorg. und Allg. Chemie*, 2009, 635, 1573–1579.

(3) Kohlmann, H. & Ritter, C. Refinement of the crystal structures of palladium-rich in-Pd compounds by X-ray and neutron powder diffraction. *Zeitschrift fur Naturforsch. - Sect. B J. Chem. Sci.*, 2007, 62, 929–934.

(4) Harris, I. R., Norman, M. & Bryant, A. W. A study of some palladium-indium, platinum-indium and platinum-tin alloys. *J. Less-Common Met.*, 1968, 16, 427–440.

(5) López, N. & Vargas-Fuentes, C. Promoters in the Hydrogenation of Alkynes in Mixtures: Insights from Density Functional Theory. *Chem. Commun.*, 2012, 48, 1379–1391.

(6) Wulff, G. XXV. Zur Frage der Geschwindigkeit des Wachsthums und der Auflösung der Krystallflächen. *Zeitschrift für Krist. - Cryst. Mater.*, 1901, 34, 449–530.

(7) Carchini, G., Almora-Barrios, N., Revilla-López, G., Bellarosa, L., García-Muelas, R., García-Melchor, M., Pogodin, S., Błoński, P. & López, N. How theoretical simulations can address the structure and activity of nanoparticles. *Top. Catal.*, 2013, 56, 1262–1272.

(8) Chou, C. W., Chu, S. J., Chiang, H. J., Huang, C. Y., Lee, C. J., Sheen, S. R., Perng, T. P. & Yeh, C. T. Temperature-programmed reduction study on calcination of nano-palladium. *J. Phys. Chem. B*, 2001, 105, 9113–9117.

(9) Frei, M. S., Capdevila-Cortada, M., García-Muelas, R., Mondelli, C., López, N., Stewart, J. A., Curulla Ferré, D. & Pérez-Ramírez, J. Mechanism and microkinetics of methanol synthesis via CO_2 hydrogenation on indium oxide. *J. Catal.*, 2018, 361, 313–321.

(10) Martin, O., Martín, A. J., Mondelli, C., Mitchell, S., Segawa, T. F., Hauert, R., Drouilly, C., Curulla-Ferré, D. & Pérez-Ramírez, J. Indium oxide as a superior catalyst for methanol synthesis by CO_2 hydrogenation. *Angew. Chemie - Int. Ed.*, 2016, 55, 6261–6265.

(11) Ebbesen, S. D., Mojet, B. L. & Lefferts, L. The influence of water and pH on adsorption and oxidation of CO on Pd/Al_2O_3-an investigation by attenuated total reflection infrared

spectroscopy. *Phys. Chem. Chem. Phys.*, 2009, 11, 641–649.

(12) Wu, Z., Wegener, E. C., Tseng, H. T., Gallagher, J. R., Harris, J. W., Diaz, R. E., Ren, Y., Ribeiro, F. H. & Miller, J. T. Pd-In intermetallic alloy nanoparticles: Highly selective ethane dehydrogenation catalysts. *Catal. Sci. Technol.*, 2016, 6, 6965–6976.

(13) Amore, S., Delsante, S., Parodi, N. & Borzone, G. Thermochemistry of Pd–In, Pd–Sn and Pd–Zn alloy systems. *Thermochim. Acta*, 2009, 481, 1–6.

Appendix E

Supporting Information to Chapter 7: Electrochemical CO_2 reduction on gas diffusion electrodes: enhanced selectivity of In-Bi bimetallic particles and catalyst layer optimization through a Design of Experiment approach

E.1 Supplementary Figures

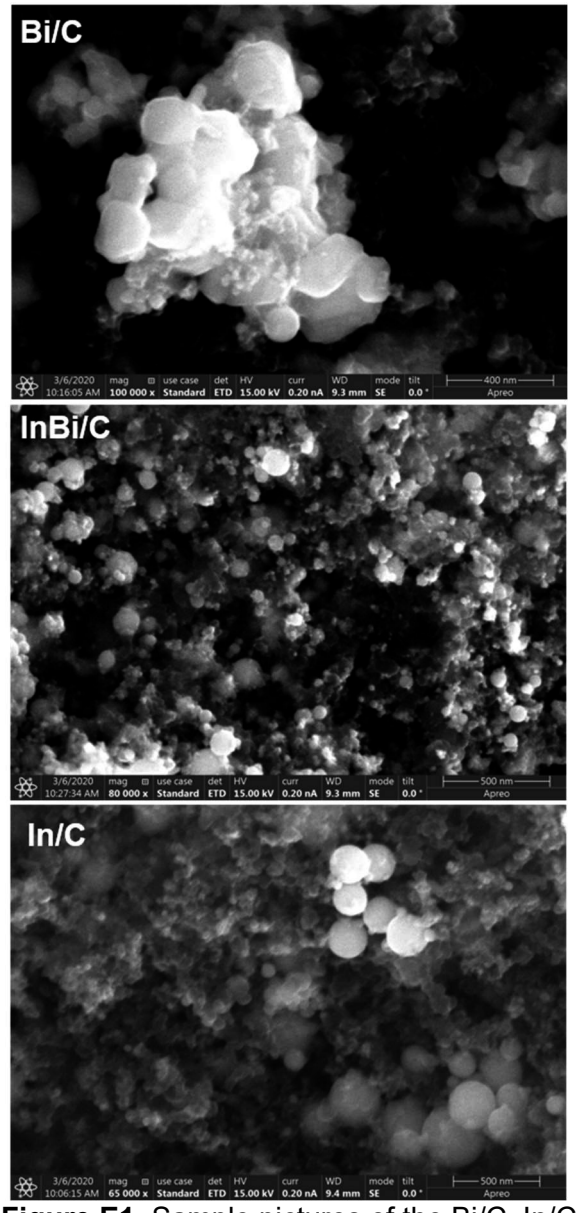

Figure E1. Sample pictures of the Bi/C, In/C and InBi/C catalysts at the loading employed for the benchmarking and characterization.

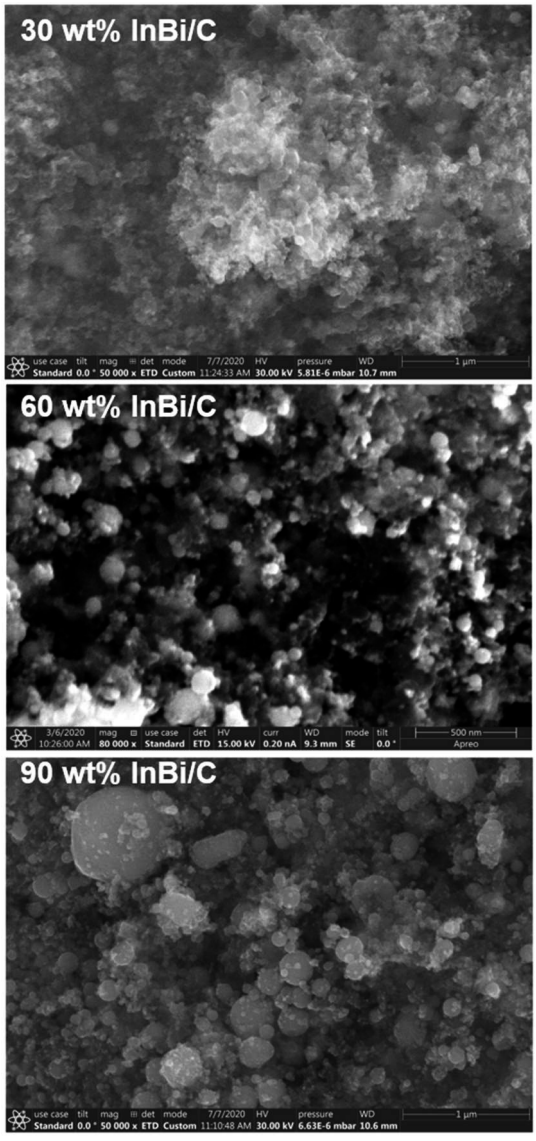

Figure E2. Sample pictures of the InBi catalyst at the three different amounts of catalyst supported on carbon investigated. It is clear that while at 30 wt% supported the catalyst particles are well dispersed on the carbon support, decreasing the amount of carbon leads to bigger particles. This, however, does not necessarily have a negative impact on performance, as it can be seen from the results of the DOE in the main text (Table 7.3).

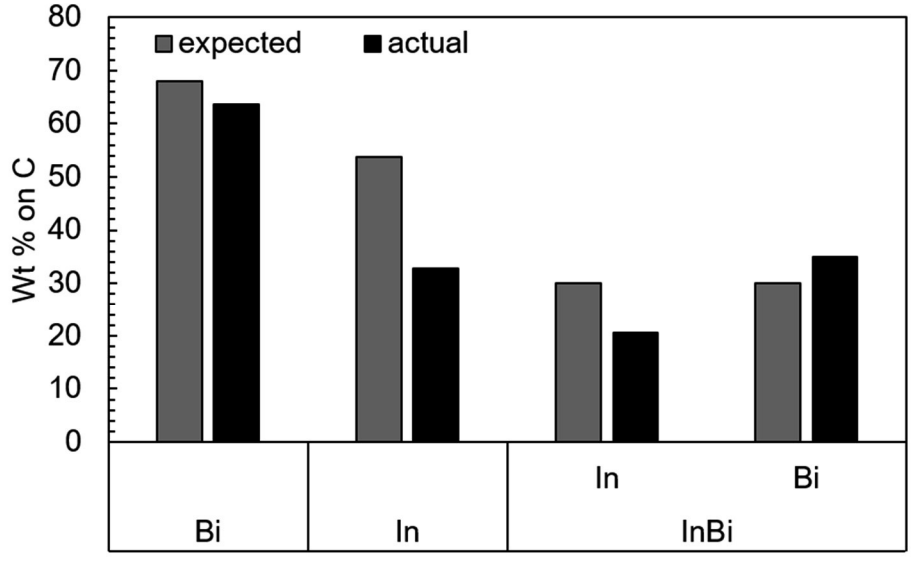

Figure E3. Expected composition and actual composition from ICP analysis. While Bi concentration is consistent with the expected one, In is lower than expected.

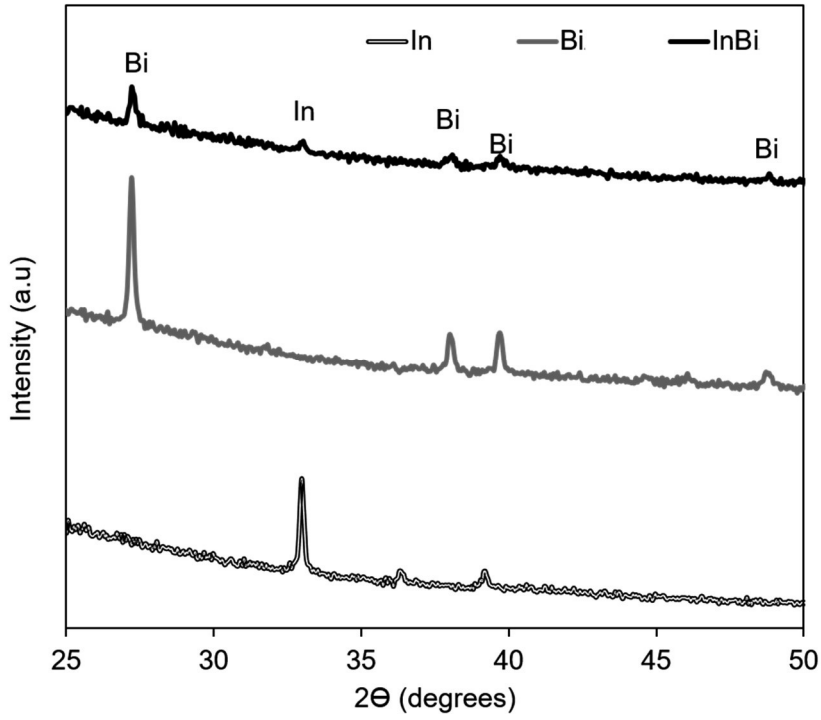

Figure E4. X-ray diffraction patterns of the three investigated catalysts.

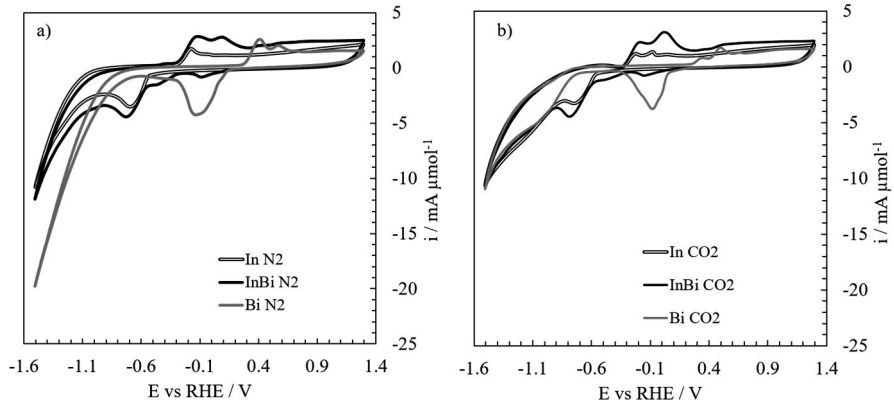

Figure E5. Stable CVs of the three catalysts in N_2 and CO_2 saturated 0.5M $KHCO_3$. Bi has a lower hydrogen evolution overpotential than In. The InBi catalyst behaves like pure In in the HER region. In the presence of CO_2 the overpotential of the cathodic reaction decreases on In and InBi, while on Bi the overall current achieved decreases.